International Journal of Applied Earth Observations and Geoinformation 98 (2021) 102298

Contents lists available at ScienceDirect

International Journal of Applied Earth Observations and Geoinformation

journal homepage: www.elsevier.com/locate/jag

Remote sensing-based actual evapotranspiration assessment in a data-scarce area of Brazil: A case study of the Urucuia Aquifer System

Bruno César Comini de Andrade [a,*], Eber José de Andrade Pinto [b,c], Anderson Ruhoff [a], Gabriel B. Senay [d]

[a] Instituto de Pesquisas Hidráulicas, Universidade Federal do Rio Grande do Sul, Porto Alegre, Brazil
[b] Escola de Engenharia, Universidade Federal de Minas Gerais, Belo Horizonte, Brazil
[c] Serviço Geológico do Brasil-CPRM, Belo Horizonte, Brazil
[d] U.S. Geological Survey (USGS) Earth Resources Observation and Science (EROS) Center, North Central Climate Adaptation Science Center, Fort Collins, CO 80523, USA

ARTICLE INFO

Keywords:
SSEBop
SMAP
GRACE
MODIS

ABSTRACT

The large groundwater reserves of the Urucuia Aquifer System (UAS) enabled agricultural development and economic growth in the western Bahia State, in northeastern Brazil. Over the last several years, concern has grown around the aquifer's diminishing water levels, and water balance (WB) studies are in demand. Considering the lack of measured actual evapotranspiration (ET_a), a major component of the water cycle, this work uses the Operational Simplified Surface Energy Balance (SSEBop) model to estimate ET_a, and compares it to basin-scale estimates from the Soil Moisture Accounting Procedure (SMAP) monthly model and from an annual WB closure method, based on gridded meteorological data and the Gravity Recovery and Climate Experiment (GRACE) product. Additionally, a comparative assessment of different versions of the SSEBop parameterization was performed. Moderate Resolution Imaging Spectroradiometer (MODIS) imagery was used to implement eight different versions of the SSEBop algorithm over the UAS between 2000 and 2013. SSEBop and SMAP ET_a yielded similar seasonal patterns, with correlation coefficient (r) up to 0.65, mean difference (MD) of 0.8 mm/month and mean absolute difference (MAD) of 18.5 mm/month. Comparison of SSEBop annual ET_a estimates to annual SMAP and WB closure estimates yielded low MD (12.1 and −7.3 mm/year, respectively) and MAD (82.5 and 82.8 mm/year, respectively), but also low r values (0.00 and 0.37, respectively). The comparison of the different SSEBop versions indicated the need to incorporate a calibration step of the aerodynamic heat resistance (r_{ah}) parameter. SSEBop results were also used for land cover and drought monitoring. Analysis indicates that agriculture, associated with an increasing trend of atmospheric evaporative demand, is responsible for the decrease in groundwater levels and streamflow in the studied time period.

1. Introduction

The Urucuia Aquifer System (UAS) is one of the largest groundwater reservoirs of Brazil, with an area close to 120,000 km^2. Water from its sandstone formations supplies the São Francisco River and is partially responsible for streamflow maintenance during the dry season (ANA, 2018). Over the last decades, the UAS native vegetation was gradually replaced by crop plantation and livestock farming. In the past few years, concern around the aquifer's ability to replenish itself has grown, as a decrease in the local rivers' baseflow and terrestrial water storage was observed (Gonçalves et al., 2019; Pousa et al., 2019). Therefore, studies about the UAS water balance are needed, since monitoring of important water cycle processes, such as actual evapotranspiration (ET_a), is scarce.

In a river basin, the main source of water loss is ET_a, a process that comprises evaporation from soil, plants and water bodies; and transpiration from plants (Tateishi & Ahn, 1996; Fisher et al., 2017). These two sub-processes occur simultaneously, making it difficult to distinguish one from the other (Allen et al., 1998). For this reason, ET_a is often addressed as a single process. Knowledge of ET_a rates is relevant both for estimates of crop consumption, at a local scale, and for assessment of water availability, at a regional scale.

Land ET_a is measured locally by flux towers and lysimeters and can

* Corresponding author.
E-mail address: cominideandrade@gmail.com (B.C.C. de Andrade).

https://doi.org/10.1016/j.jag.2021.102298
Received 23 October 2020; Received in revised form 30 December 2020; Accepted 31 December 2020
Available online 29 January 2021

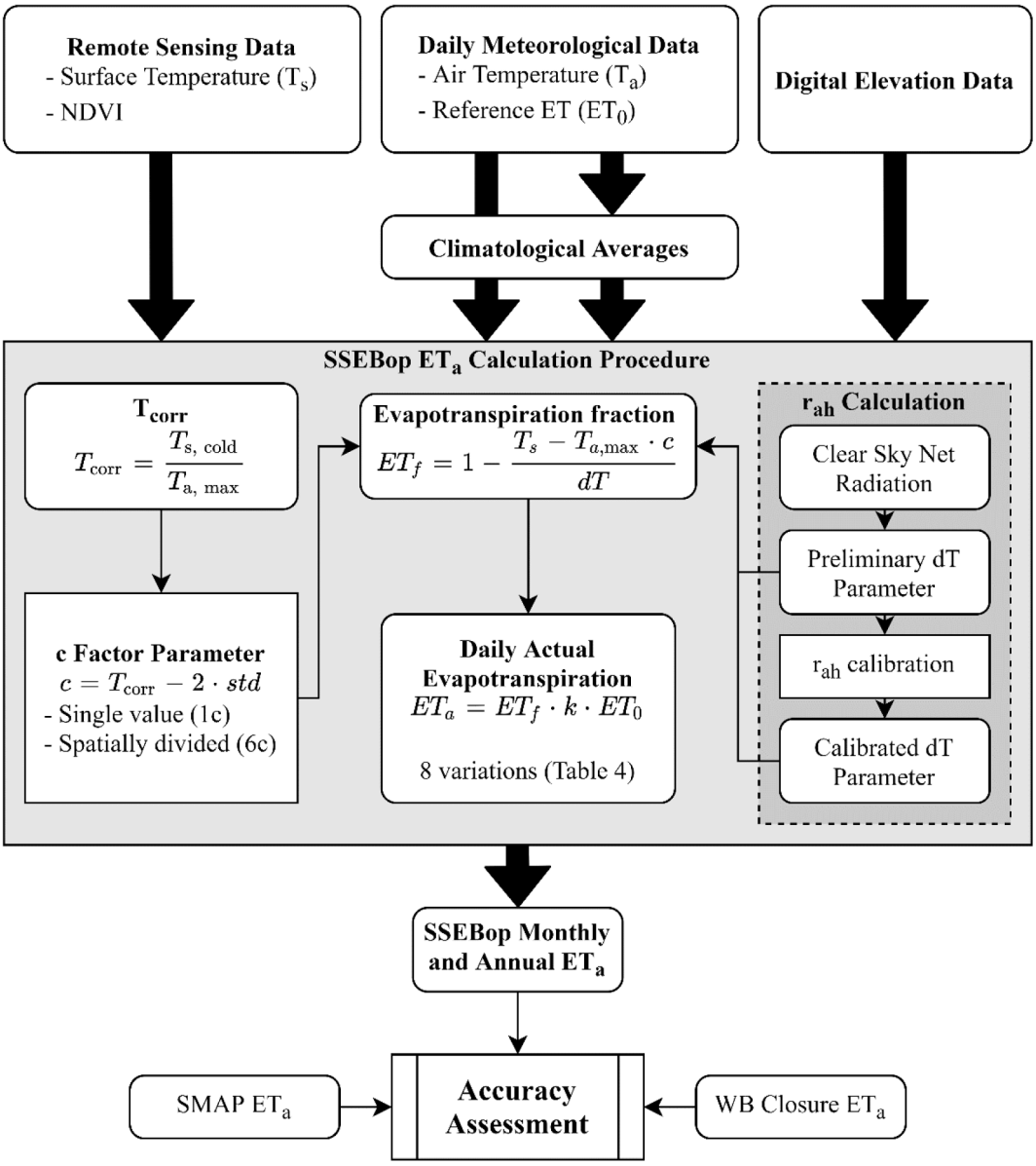

Fig. 1. Simplified flowchart SSEBop ET_a calculation procedure and assessment.

also be estimated from meteorological and hydrological processes. However, these measurements only represent local processes and can rarely be extended to large areas due to land cover heterogeneity (Kalma et al., 2008). To estimate ET_a over large areas, surface energy balance (SEB) models and water balance (WB) models are commonly used (Liou & Kar, 2014).

Despite their simplicity, lumped WB models, such as the Soil Moisture Accounting Procedure – SMAP (Lopes et al., 1982), provide accurate results and can be used to investigate ET_a rates, among other hydrological processes within a river basin at daily and monthly time intervals (Alley, 1984; Guo et al., 2017). In addition, the Gravity Recovery and Climate Experiment (GRACE) has also shown great potential as a reference tool for WB closure at large scales (Wouters et al., 2014). The GRACE mission (Tapley et al., 2004) computes Total Water Storage Anomaly (TWSA) by indirectly measuring spatial changes of Earth's gravity (Schmidt et al., 2008). Over the last two decades, GRACE measurements have been used to monitor extreme events, such as droughts (Chen et al., 2009; Xavier et al., 2010) and monsoons (Nahmani et al., 2012; Fu et al., 2013), as well as to improve estimates of water balance processes (Moreira et al., 2019; de Sales & Rother, 2020).

Although WB models can indirectly provide ET_a values at the basin scale with high accuracy, they do not capture the process's high spatial variability. On the other hand, advances in remote sensing technology has enabled the creation of SEB-based models that provide spatial and temporal estimates of ET_a with reasonable accuracy, both at local and regional scales (Opoku-Duah et al., 2008; Li et al., 2009). Among such models, the Operational Simplified Surface Energy Balance (SSEBop) model is relatively simple to implement (Senay et al., 2013), but has provided accurate ET_a estimates over a wide range of climates across the globe (Chen et al., 2016; Senay et al., 2017; Alemayehu et al., 2017; Paula et al., 2019; Dias Lopes et al., 2019; Senay et al., 2020). However, even in light of the different SSEBop applications found in the literature, a comparative study of the various possible model parameterizations and driving datasets is still lacking.

In this paper, we aimed to assess SSEBop ET_a estimates over the UAS, a region that, despite its economic and hydrological relevance, lacks proper monitoring of ET_a. In this context, we performed a comparative study of eight SSEBop versions, and validated the estimates against the ET_a estimates from the SMAP model and from WB closure using GRACE and local meteorological data. The SSEBop model was then used for land

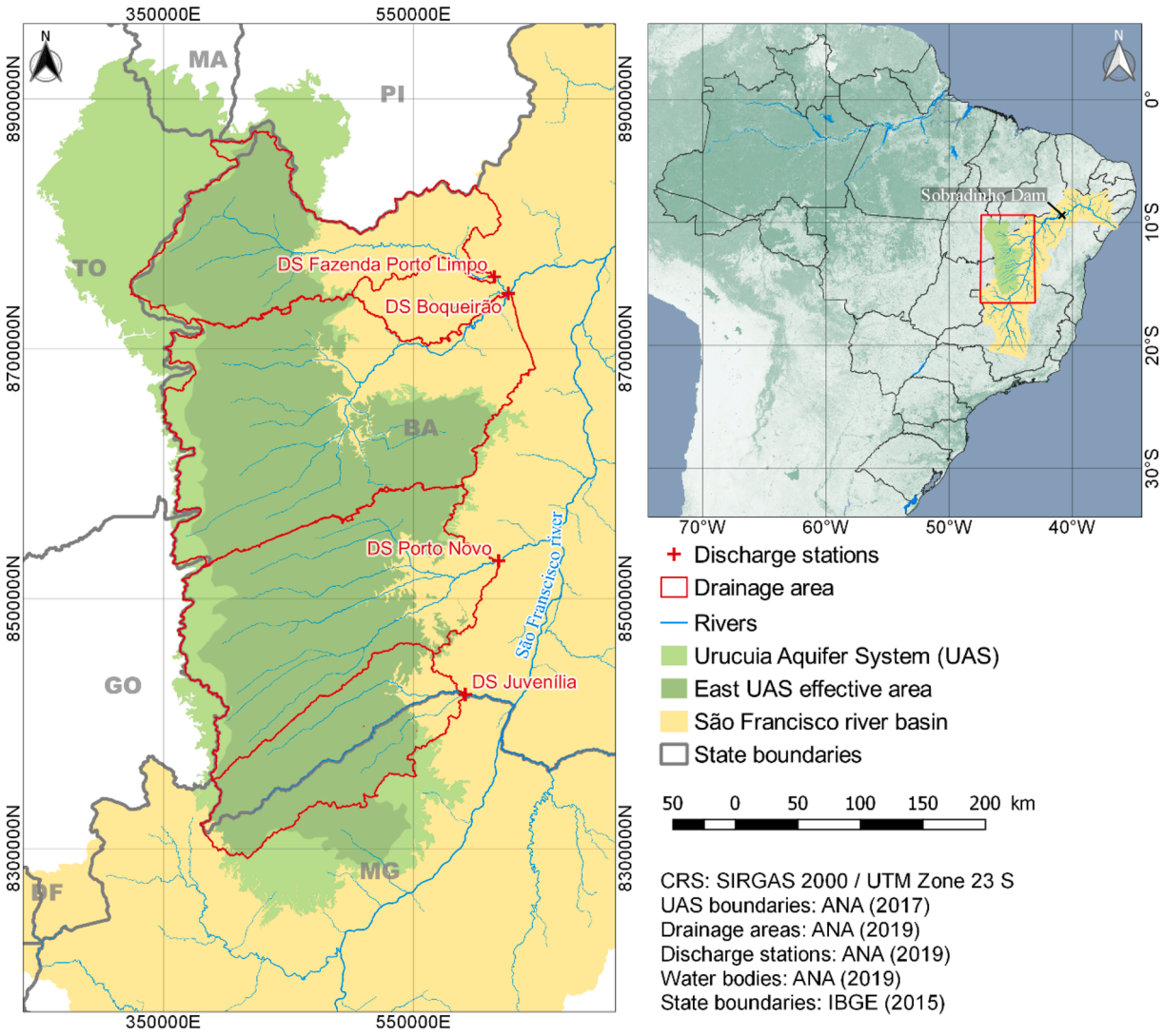

Fig. 2. São Francisco River basin, UAS location and modeled river basins distribution.

cover and drought monitoring between 2000 and 2013.

2. Material and methods

The SSEBop model (Senay, 2018) was applied with the Moderate Resolution Imaging Spectroradiometer (MODIS) data in the region of the UAS, and then compared to SMAP and WB closure ET_a, on four river basins. Fig. 1 presents a simplified flowchart of the model implementation and evaluation. A total of eight versions of SSEBop ET_a were evaluated, considering meteorological or climatological input datasets, zone splitting of the temperature correction factor (c factor) parameter, and calibration of the aerodynamic heat resistance (r_{ah}) parameter. Accuracy assessment of the SSEBop estimates was performed by means of dual evaluation. ET_a derived from SSEBop was aggregated into monthly and annual estimates and spatially averaged for each evaluated river basin. Then, SSEBop ET_a was compared to the SMAP and WB closure estimates.

2.1. Study area

Located in northeastern Brazil, the UAS covers part of 6 Brazilian States and is one of the country's largest groundwater reservoirs, as seen in Fig. 2. The east UAS effective area, which is responsible for the baseflow of the São Francisco River tributaries, is presented as well (Gaspar & Campos, 2007). The aquifer's baseflow is responsible for more than 40% of São Francisco River flow, measured at Sobradinho Dam, to the northeast, and also feeds the Tocantins River tributaries, to the west (ANA, 2017).

The study area climate is predominantly tropical with two well-defined seasons: a dry and mild season (April-September), and a wet and hot season (October-March) (Alvares et al., 2013). Averaging 1100 mm of annual precipitation, 80% of rainfall occurs between November and March, with almost no precipitation between June and August (INMET, 2019). Despite the seasonal pattern of rainfall, rivers in the region are perennial, which can be associated with the UAS capacity to sustain baseflow throughout the dry season (Gaspar & Campos, 2007; Gonçalves et al., 2018). Average air temperature ranges between 20 °C and 30 °C, with July and October as the coldest and hottest months, respectively (INMET, 2019).

Fig. 3 displays land cover changes that occurred in the region between 2001 and 2013. Cropland areas in the UAS nearly doubled, growing from around 9.3 thousand km^2 in 2001 to over 16.1 thousand km^2 in 2013. Irrigated area has grown as well, increasing from less than 15 km^2 in 1985 to more than 1670 km^2 in 2016 (Guimarães et al., 2017). Nevertheless, there is a growing concern over the sustainable supply of fresh water and hydroelectric power generation, as a reduction in rainfall (up to 12%) and in streamflow (up to 60%) has been identified over the past three decades (Pousa et al., 2019). Additionally, an

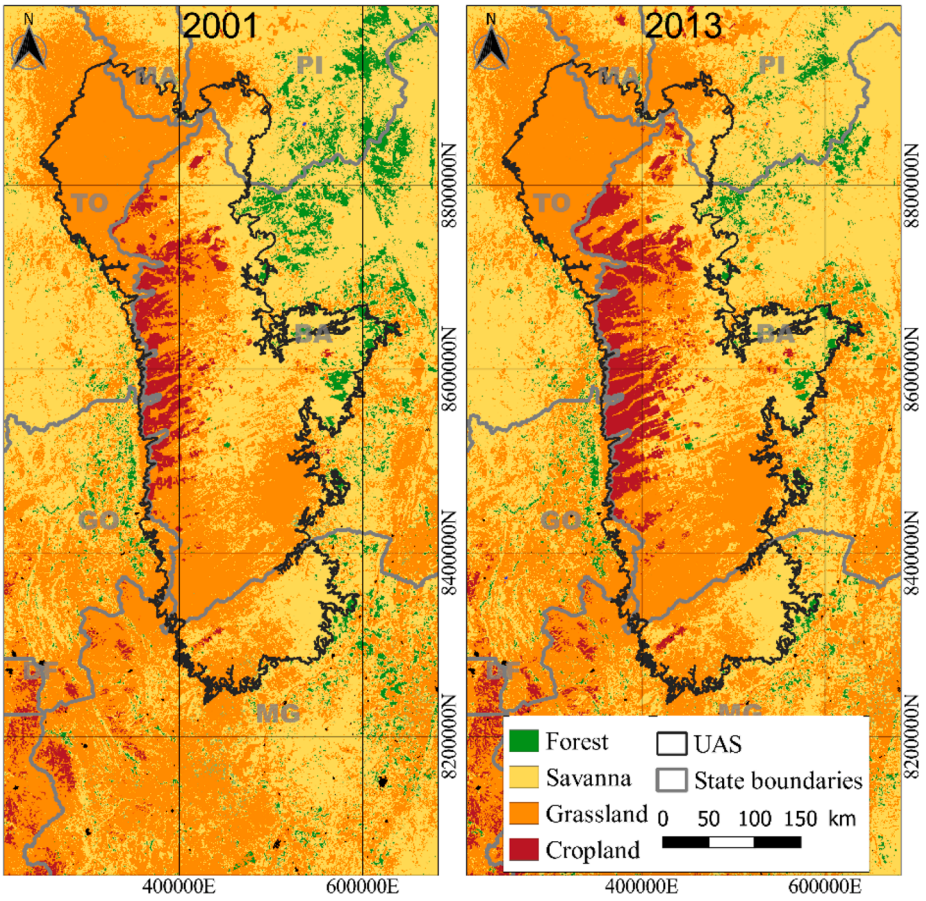

Fig. 3. UAS land cover change between 2001 and 2013, derived from the MCD12Q1 v006 product. Data source from Friedl & Sulla-Menashe (2019).

Table 1
Input datasets used in the SSEBop implementation.

Input Datasets	Symbol	Source	Resolution	
			Spatial	Temporal
Surface elevation	Z	GMTED2010 (Danielson & Gesch, 2011)	900 m	–
Surface temperature	T_s	MODIS TERRA (Wan, 2015)	1000 m	1 day
Normalized Difference Vegetation Index	NDVI	MODIS TERRA (Didan, 2015)	1000 m	16 days
Reference evapotranspiration	ET_0	(Xavier et al., 2015)	27 km	1 day
Max daily air temperature	T_{max}	(Xavier et al., 2015)	27 km	1 day
Min daily air temperature	T_{min}	(Xavier et al., 2015)	27 km	1 day

Table 2
Datasets used in the water balance modeling.

Input Datasets	Symbol	Source	Resolution	
			Spatial	Temporal
Precipitation	P	(Xavier et al., 2015)	27 km	1 day
Observed streamflow	Q	(ANA, 2019)	–	1 day
Total Water Storage Anomaly	TWSA	GRACE TELLUS (Swenson, 2012)	110 km	monthly
Reference evapotranspiration	ET_0	(Xavier et al., 2015)	27 km	1 day

increasing trend in pan evaporation (Althoff et al., 2019) and air temperature (de Jong et al., 2018) further escalate the pressure on the aquifer.

2.2. Input dataset

Table 1 presents the input dataset used in the SSEBop implementation over the UAS region, while Table 2 shows the dataset utilized in the WB modeling. For the spatiotemporal analysis of ET_a, land cover data from the MCD12Q1 v006 product (Friedl & Sulla-Menashe, 2019) was used between 2001 and 2013.

2.3. The SSEBop model

Developed by Senay et al. (2013), SSEBop uses remote sensing multispectral data and ancillary meteorological data to derive the surface ET_a, as given by Eq. (1):

$$ET_a = ET_f \cdot k \cdot ET_0 \quad (1)$$

where ET_f is the evapotranspiration fraction; ET_0 is the reference evapotranspiration for grass surface (mm/day); and k is a scaling factor. A predefined value of k factor = 1.20 is used (Senay et al., 2013; Senay, 2018), which simulates an aerodynamically rougher surface than the grass reference, such as alfalfa.

For a given image, each pixel's ET_f is derived from the relationship between surface temperature (T_s), and the temperatures of cold (T_c) and hot (T_h) boundary conditions.

The ET_f is given by Eq. (2):

$$ET_f = \frac{T_h - T_s}{T_h - T_c} = 1 - \frac{1}{dT}(T_s - T_c) \quad (2)$$

Table 3
Evaluated SSEBop ET_a estimation versions for r_{ah}, input datasets and number of c factor zones.

SSEBop Version	Aerodynamic Resistance (s/m)	Input Dataset	c factor
p1	110	Meteorological	One zone
p2	110	Meteorological	Six zones
p3	110	Climatological	One zone
p4	110	Climatological	Six zones
p5	Calibrated	Meteorological	One zone
p6	Calibrated	Meteorological	Six zones
p7	Calibrated	Climatological	One zone
p8	Calibrated	Climatological	Six zones

where T_s is the surface temperature of a pixel; T_h is the estimated surface temperature of the hot (dry) boundary condition for the same pixel; T_c is the surface temperature of the cold (wet) boundary condition for the pixel; and dT is the pixel temperature difference between boundary conditions T_c and T_h ($dT = T_h - T_c$). Negative ET_f values are converted to zero, while the maximum ET_f value is capped to 1.05. Pixels with cloud presence, identified in the MODIS product or defined by the Senay (2018) methodology, were removed from analysis.

The value of T_c is calculated from air temperature, according to Eq. (3):

$$T_c = \text{cfactor} \cdot T_{max} \tag{3}$$

where T_{max} is daily maximum air temperature; and c is a correction factor that relates T_{max} and T_s in a well vegetated surface with good water availability. Senay et al. (2017) defined how to calculate c factor, according to Eqs. (4) and (5):

$$T_{corr} = \frac{T_{s\_cold}}{T_{max}} \tag{4}$$

$$\text{cfactor} = T_{corr,mean} - 2 \cdot T_{corr,std} \tag{5}$$

where T_{s_cold} is the surface temperature in well vegetated places, in which the Normalized Difference Vegetation Index (NDVI) is equal to or greater than 0.7; T_{corr} is the ratio between T_s and T_{max} in well vegetated places; and $T_{corr,mean}$ and $T_{corr,std}$ respectively refer to the spatial average (mean) and standard deviation (std) of T_{corr} pixels for a given image. For each image, a minimum of 50 T_{corr} pixels was used, as recommended by Senay et al. (2017). For images that failed this criterion, a historical average of c factor (2000–2013) was used.

The dT parameter is calculated as a solution of the energy balance equation for exposed and dry soil, which represents the dry (hot) boundary condition. For the calculation of dT, we consider latent heat flux (LE) and soil heat flux (G) are equal to zero, as proposed by Senay et al. (2013), so that dT is given by Eq. (6).

$$dT = \frac{R_n \cdot r_{ah}}{\rho_a \cdot C_p} \tag{6}$$

where R_n is the net radiation; H is the sensible heat flux; ρ_a is the specific mass of air; C_p is the specific heat of air; and r_{ah} is the aerodynamic heat resistance for exposed and dry soil. Senay et al. (2013) determined the value of r_{ah} via calibration in the United States and recommended $r_{ah} = 110$ s/m, which corresponds to the aerodynamic resistance over exposed soil. R_n, ρ_a and C_p are derived from formulations given by Allen et al. (1998), under the assumption of clear-sky conditions.

To evaluate the effects of model parameterization and choice of input datasets, eight SSEBop versions were applied in this work, as listed in Table 3. The versions are distinguished by the value of the r_{ah} parameter (110 s/m or a calibrated value), by input dataset (meteorological or climatological dT and ET_0) and by spatial distribution of the c factor. Details on the parameterization of the different versions is presented in **Appendix A**.

Table 4
Selected fluviometric stations information.

Station Code	Station Name	River	Drainage Area (km^2)	
			Topographic	Subterranean
46870000	Fazenda Porto Limpo (FPL)	Preto	22,470	22,210 (98.8%)
46902000	Boqueirão (BOQ)	Grande	41,935	38,745 (92.4%)
45960001	Porto Novo (PNV)	Corrente	31,435	28,515 (90.7%)
45260000	Juvenília (JUV)	Carinhanha	16,440	16,180 (98.4%)

2.4. Basin-scale water balance

SSEBop ET_a estimates were compared to ET_a estimates derived from the water balance in four river basins. These basins were chosen because their drainage areas encompass most of the East UAS area and present consistent streamflow gauged data at four discharge stations (DS) between 2000 and 2012 (ANA, 2019). Fig. 2 displays the river basins (i.e., drainage areas), as well as their DS locations, and Table 4 presents additional information about the selected river basins and DS. Topographic (superficial) and subterranean drainage areas (UAS effective area) are discriminated in Table 4. The percentage of subterranean contribution area for each river basin is displayed as well.

The SMAP model was used to calculate ET_a at monthly and annual time intervals, while WB closure was applied to calculate ET_a at annual time intervals. Given the seasonality patterns of the hydrological variables in the UAS region, annual fluxes were calculated considering the hydrological year, which starts in July of one year and ends in June of the next year. Details on the application of the SMAP model and the WB closure are presented in **Appendix B**.

2.5. ET_a estimates analysis and comparison

ET_a derived from the eight SSEBop versions was compared at monthly and annual time intervals to ET_a from the SMAP model, and at annual time intervals to ET_a from WB closure. Alongside seasonal and annual time series charts, statistical metrics were used for the comparison. Eqs. (7)–(9) present the metrics used:

$$r = \frac{\sum (x_i - x_{avg})(y_i - y_{avg})}{\sqrt{\sum (x_i - x_{avg})^2 \sum (y_i - y_{avg})^2}} \tag{7}$$

$$MD = \frac{\sum (x_i - y_i)}{n} \tag{8}$$

$$MAD = \frac{\sum |x_i - y_i|}{n} \tag{9}$$

where r is the correlation coefficient; x_i is one SSEBop ET_a estimate; x_{avg} is the average of SSEBop ET_a estimates; y_i is one SMAP or WB closure ET_a estimate; y_{avg} is the average of SMAP or WB closure ET_a estimates; n is the number of observations; MD is the mean difference; and MAD is the mean absolute difference. The metrics were calculated for the spatial average of ET_a among the four studied river basins.

Trends and standard errors of trends of the hydrological variables were calculated using the ordinary least squares (OLS) method. Trend statistical relevance was assessed based on the modified Mann-Kendall test (Yue & Wang, 2004), at a 5% significance level.

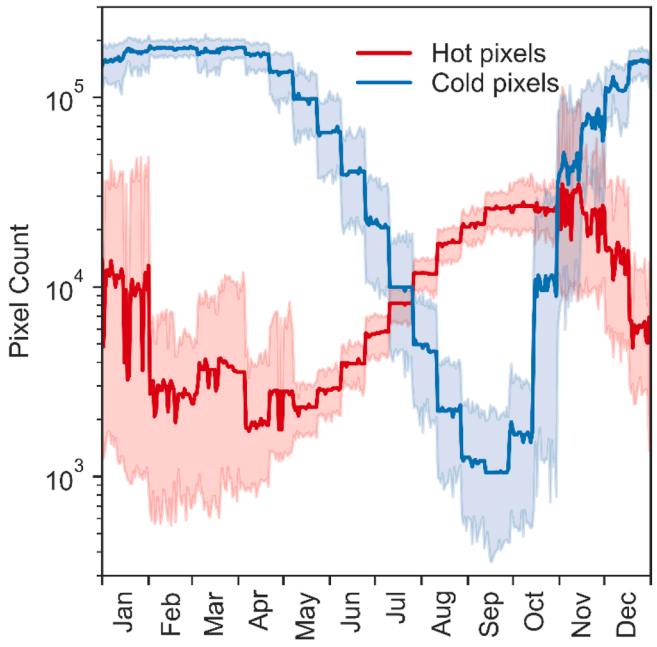

Fig. 4. Hot and cold pixels count for each UAS image between April 2000 and December 2013, presented for each day of the year (DOY). Shaded areas represent the difference between maximum and minimum pixel count for each DOY.

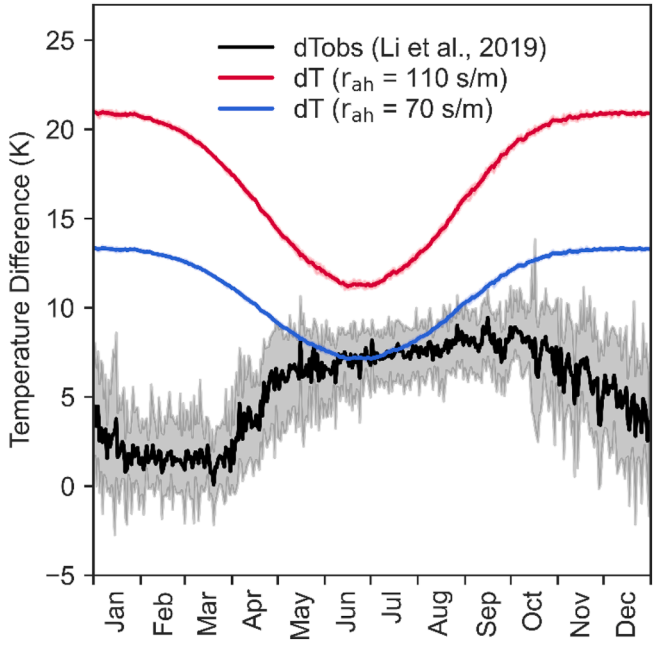

Fig. 5. Comparison of observed (black) and calculated dT with r_{ah} = 110 s/m (red) and r_{ah} = 70 s/m (blue), presented for each day of the year (DOY). Shaded areas represent the difference between maximum and minimum observed dT for each DOY. (For interpretation of the references to colour in this figure legend, the reader is referred to the web version of this article.)

3. Results

3.1. SSEBop model results

3.1.1. dT validation

For each T_s image, we used T_h and T_c criteria defined by Ji et al. (2019) to calculate observed dT (dT_{obs}) over the entire UAS region. Fig. 4 displays the pixel count seasonal distribution. Cold and hot pixels' frequencies present opposite seasonal behavior, with cold pixels maxing out in the wet season (peaking by the end of February) and reaching the bottom by the end of the dry season (September).

Fig. 5 shows the seasonal values of dT_{obs}, dT calculated with r_{ah} = 110 s/m, as recommended by Senay et al. (2013) and dT after r_{ah} calibration. Calibration resulted in r_{ah} = 70 s/m. Uncalibrated r_{ah} resulted in overestimated dT, while the calibrated r_{ah} yielded dT estimations closer to dT_{obs}. It is worth mentioning that dT and dT_{obs} have opposite seasonal behavior. This happens because water availability during the wet season (October-March) greatly reduces the T_s difference between densely and sparsely vegetated areas. The utilization of meteorological or climatological input data did not affect significantly the calibration step and resulted in the same value for r_{ah}.

3.1.2. SSEBop versions comparison

SSEBop ET_a was calculated according to the eight versions presented in Table 3. Fig. 6 displays a comparison of the results. ET_a varies seasonally, presenting lower values during the dry season, reaching the bottom in July, and higher values in the wet season, peaking in January.

SSEBop ET_a is sensitive to r_{ah} calibration, as versions with higher r_{ah} yielded approximately 30% higher ET_a in relation to those with lower r_{ah} value (Fig. 6A and B). Input data are also relevant, as meteorological versions yield higher ET_a seasonal variability, with higher ET_a values during the wet season (October to March) (Fig. 6C), and are more sensitive to daily variations of the inputs (Fig. 6D). Versions with c factor split into 6 zones per image yielded higher ET_a estimates than those yielded with a single c factor zone per image. The difference is more significant in the dry season, when ET_a estimates are lower (Fig. 6E and F).

3.2. Comparison of remote sensing and water balance ET_a

Table 5 presents the comparison metrics between SSEBop, SMAP and WB closure ET_a estimates. At monthly time intervals, the eight versions of SSEBop presented similar correlation (r between 0.57 and 0.65), but versions that used uncalibrated r_{ah} (from p1 to p4) presented significantly higher MD and MAD values. SSEBop version p5 (calibrated r_{ah}, meteorological data, one c factor zone) presented both the highest correlation and the lowest MD and MAD. At annual time intervals, SSEBop versions that used climatological data (p3, p4, p7 and p8) presented higher correlation, and lower MD and MAD. In general, SSEBop estimates presented higher correlation to WB closure ET_a than to SMAP estimates. Versions with calibrated r_{ah} (from p5 to p8) yielded lower MD and MAD values. SSEBop version p5 presented the closest ET_a estimates to both SMAP and WB closure ET_a, although the correlation values were lower than those of versions with climatological input data (p3, p4, p7 and p8). Comparison between SMAP and WB closure annual ET_a estimates yielded r = 0.40, MD = 7.8 mm/year and MAD = 72.7 mm/year.

Fig. 7 displays SMAP and SSEBop seasonal monthly ET_a, as well as SMAP uncertainties (shaded area). SMAP and SSEBop both yielded similar seasonal amplitude of ET_a. While SSEBop versions p1 to p4 generally yielded higher ET_a throughout the year, versions p5 to p8 yielded closer estimates to SMAP ET_a, staying within SMAP uncertainty boundaries for most of the year. SSEBop version p5 more closely adheres to SMAP seasonal ET_a.

Given its closer adherence to SMAP seasonal ET_a, SSEBop version p5 (calibrated r_{ah}, meteorological data, one c factor zone) was selected for further comparisons. Fig. 8 presents annual (A) and seasonal (B) values of precipitation (P), streamflow (Q), total water storage variation (ΔS), total water storage anomaly (TWSA), Normalized Difference Vegetation Index (NDVI), reference evapotranspiration (ET_0), evapotranspiration fraction (ET_f) and actual evapotranspiration (ET_a) for hydrological years between 2000 and 2013. Hydrological years extend between July of one year and June of the next year. A strong positive correlation was identified between P and WB closure ET_a (r = 0.85); Q and TWSA (r = 0.76);

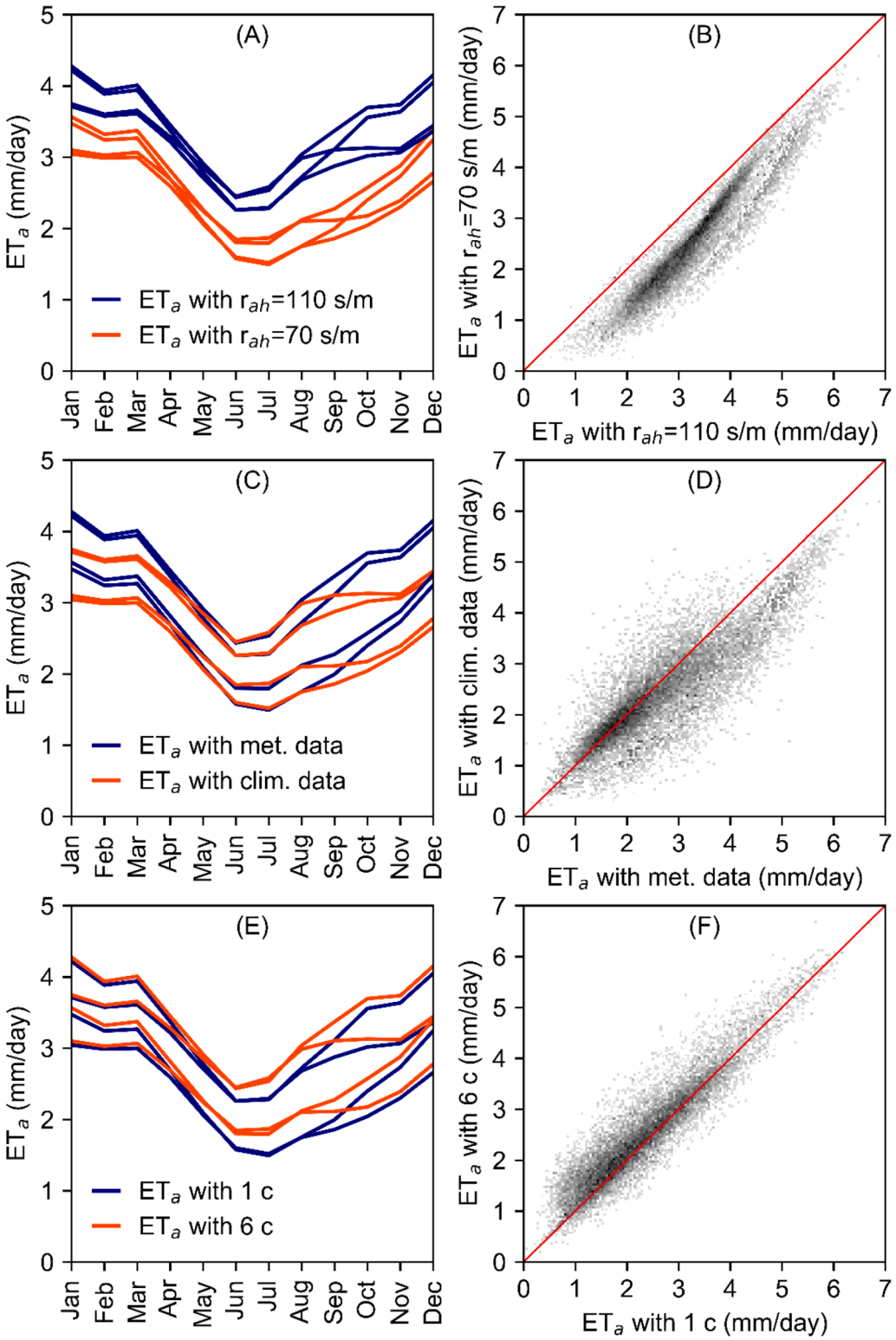

Fig. 6. Summary of the eight SSEBop versions results in the UAS. Seasonal estimations and scatter plots are displayed comparing: uncalibrated and calibrated r_{ah} (A and B); meteorological and climatological input data (C and D); single and multiple c factor zones (E and F).

and NDVI and ET_f (r = 0.71). Similar seasonal patterns were yielded by TWSA, NDVI and ET_f. On the other hand, ET_0 yielded a negative correlation to all other variables, and an opposite seasonal pattern.

Table 6 presents the trends of P, Q, TWSA, NDVI, ET_0, ET_f, and ET_a, during the common data period (2002–2012), and their standard errors. No significant trend was observed for P, ET_f, and WB closure ET_a. NDVI, ET_0, SMAP and SSEBop ET_a yielded positive trends. Significant decreasing trends were observed for Q and TWSA.

3.3. Using the SSEBop model results for land cover and drought monitoring

Based on the analysis of the different versions of the SSEBop model and on the comparison to SMAP ET_a and Grace ΔS and TWSA, version p5

Table 5
Comparison metrics between the SSEBop versions estimates and monthly ET_a from SMAP and annual ET_a from SMAP and GRACE.

SSEBop version	Comparison to SMAP Monthly ET_a			Comparison to SMAP Annual ET_a			Comparison to GRACE Annual ET_a		
	r	MD $\left(\frac{mm}{month}\right)$	MAD $\left(\frac{mm}{month}\right)$	r	MD $\left(\frac{mm}{year}\right)$	MAD $\left(\frac{mm}{year}\right)$	r	MD $\left(\frac{mm}{year}\right)$	MAD $\left(\frac{mm}{year}\right)$
p1	0.64	32.2	34.6	−0.08	388.4	388.4	0.28	369.3	372.7
p2	0.63	37.1	38.9	−0.05	449.1	449.1	0.29	427.9	431.4
p3	0.62	19.1	28.1	0.32	230.6	230.6	0.63	216.9	220.7
p4	0.57	23.9	31.8	0.40	289.2	289.2	0.64	273.5	273.9
p5	0.65	0.8	18.5	0.00	12.1	82.5	0.37	−7.3	82.8
p6	0.64	7.0	19.8	0.00	88.8	108.5	0.41	65.7	98.9
p7	0.64	−8.9	19.1	0.35	−106.9	116.0	0.59	−119.0	122.1
p8	0.60	−3.1	19.8	0.45	−35.0	63.8	0.61	−50.4	81.5

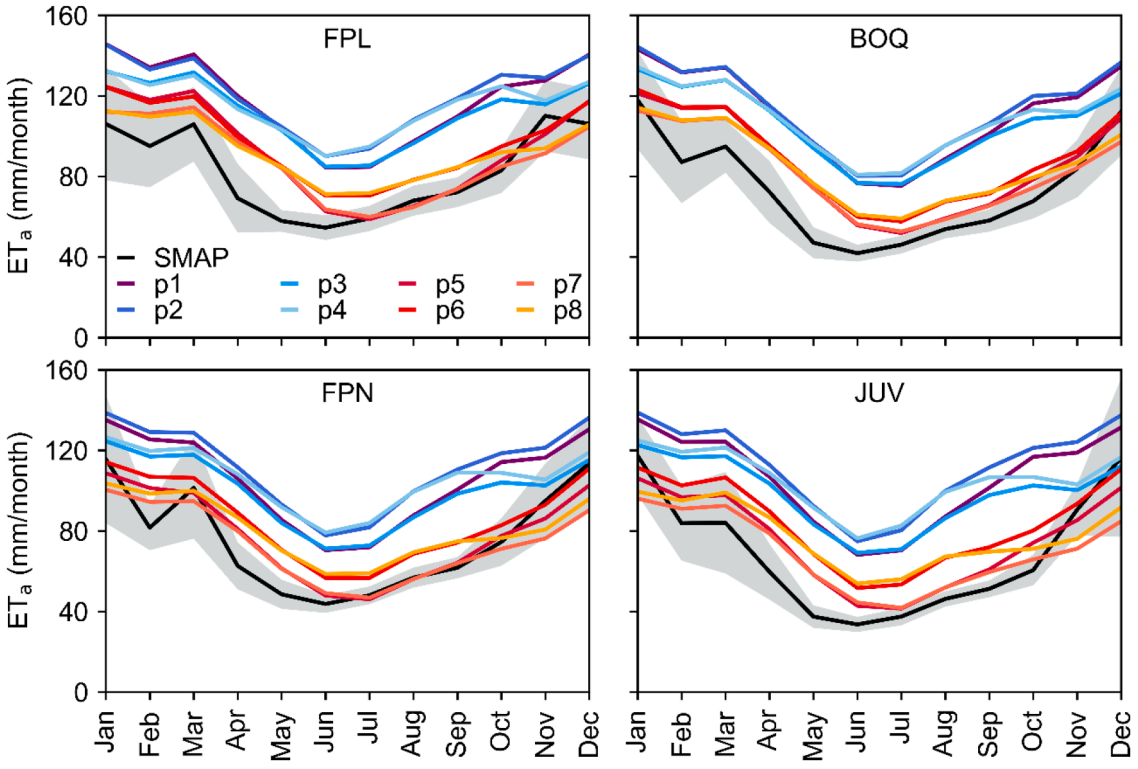

Fig. 7. Monthly ET_a over four studied watersheds, derived by SMAP and the eight SSEBop versions. The shaded area represents uncertainties in SMAP ET_a.

(calibrated r_{ah}, meteorological inputs, single c factor per image) was chosen for land cover and drought observations.

Fig. 9 shows the expansion of croplands in the UAS, from 9400 km^2 in 2001 to 16,200 km^2 in 2013 (A). An area of almost 7000 km^2, composed of grassland (94.3%) and savanna (5.7%), went through a gradual transition to croplands (B). Seasonal patterns (C) and annual anomalies (D) also gradually became similar to that of croplands, with larger seasonal amplitude and less sensitivity to water availability.

ET_a over natural land covers (forest, savanna and grassland) in the UAS has a similar seasonal amplitude of about 50 mm/month, but different average values, with forest having the highest ET_a and grassland the lowest. On the other hand, cropland ET_a presents a larger seasonal amplitude, being higher than that of savanna in the first quarter and lower than grassland for the rest of the year.

In the UAS, ET_a in croplands yielded an increasing trend (4.7 ± 3.4 mm/year), while in grassland ET_a yielded a decreasing trend (-4.4 ± 3.4 mm/year). The cropland expansion area, and the savanna and forest land covers yielded no significant trend of ET_a (2.2 ± 3.3 mm/year, 1.2 ± 5.0 mm/year and −1.9 ± 4.6 mm/year, respectively). Annual ET_a in croplands and in the cropland expansion area yielded negative correlation to P (r = -0.21 and r = -0.28, respectively) and positive correlation to ET_0 (r = 0.39 and r = 0.33, respectively) in the UAS. Cropland ET_a also seems to be less sensitive to water scarcity, as it yielded positive anomalies during the 2007–2008 hydrological year.

In this work, the SSEBop ET_f was used to monitor drought. Fig. 10 presents the average monthly ET_f over the UAS, for each month of the year, derived between April-2000 and December-2013. A higher spatial variation is observed during the dry season (April-September), when cropland areas yield ET_f lower than 0.2 while in forested areas it remains higher than 0.6. During the wet season (October-March), most of the UAS yields ET_f higher than 0.4.

Fig. 11 presents the average annual ET_f over the UAS (2000–2013) as well as the annual anomalies per hydrological year, between 2000 and 2013. Savanna and forest (eastern UAS) ET_f anomalies indicate that these land covers are more sensitive to rainfall anomalies, such as the drought of 2001–2003 (Bazame et al., 2018) and the dry summer of 2007–2008 (Sun et al., 2016); and the period of 2011–2013, which coincides with a decreasing trend in both NDVI and TWSA.

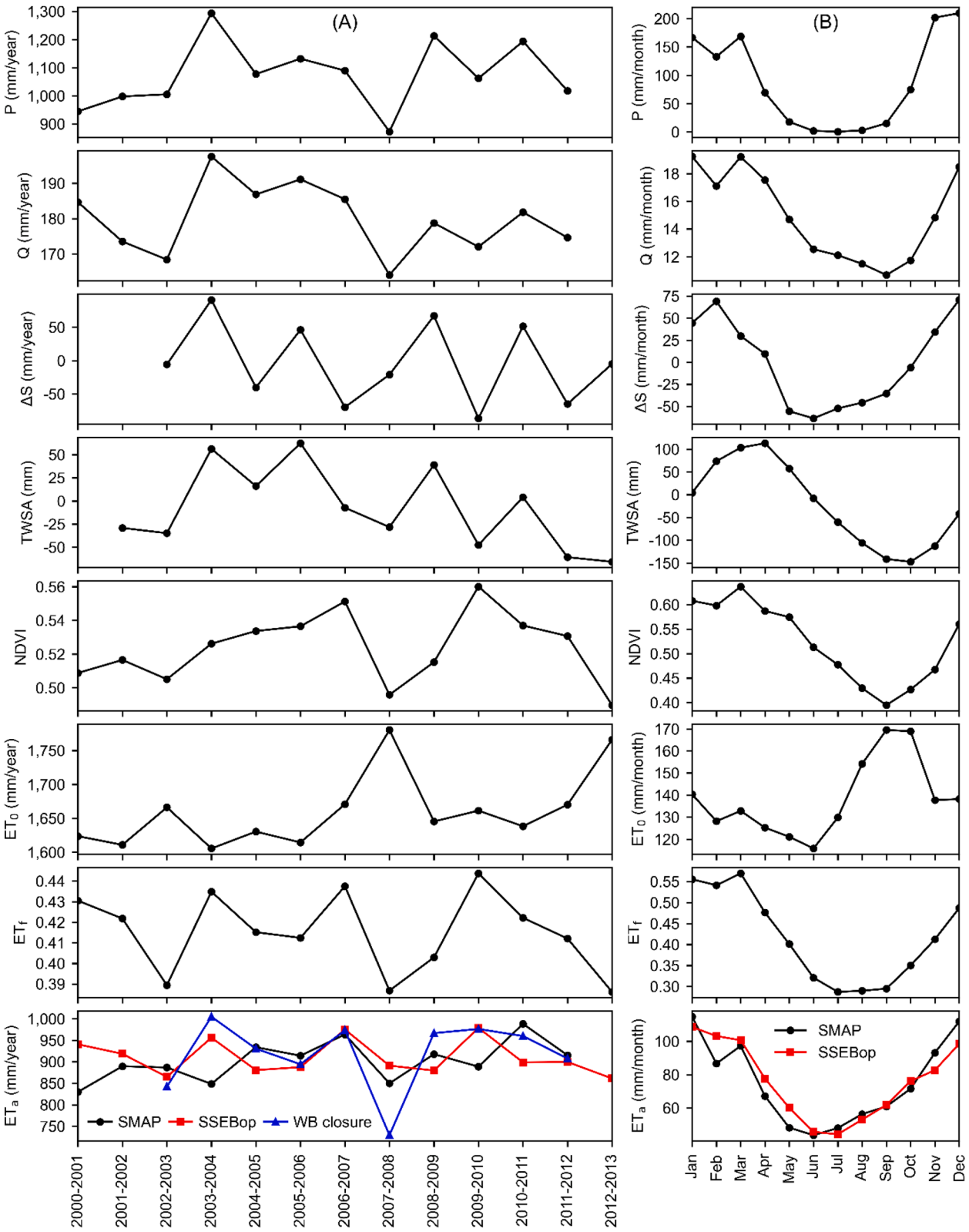

Fig. 8. Time series of precipitation (P), streamflow (Q), total water storage variation (ΔS), total water storage anomaly (TWSA), Normalized Difference Vegetation Index (NDVI), reference evapotranspiration (ET_0), evapotranspiration fraction (ET_f) and actual evapotranspiration (ET_a) for hydrological years from 2000 to 2013 (A) and the respective mean seasonal cycles (B).

Table 6
Spatial averaged annual trends of the hydrological variables and their statistical significance, for the common data availability period (2002–2012).

Variable (unit)	Trend ± Standard error	Significant trend
P (mm/year)	−3.9 ± 13.9	No trend
Q (mm/year)	−1.1 ± 1.2	Decreasing
TWSA (mm/year)	−6.1 ± 4.6	Decreasing
NDVI (-)	0.002 ± 0.002	Increasing
ET_0 (mm/year)	3.8 ± 5.5	Increasing
ET_f (-)	0.001 ± 0.002	No trend
SMAP ET_a (mm/year)	5.5 ± 4.9	Increasing
WB closure ET_a (mm/year)	2.9 ± 9.5	No trend
SSEBop ET_a (mm/year)	1.8 ± 4.9	Increasing

4. Discussion

4.1. SSEBop uncertainty assessment

4.1.1. SSEBop uncertainty related to aerodynamic resistance

Ji et al. (2019) proposed a method to validate SSEBop dT estimates and indicated that the model's dT estimation was reliable. However, we have found that SSEBop dT estimates are higher than the observed in the UAS. This difference in dT may lead to overestimation of ET_a. The value of r_{ah} varies greatly, driven mainly by wind speed, and lower values of r_{ah} (around 70 s/m) are common during daylight hours on both bare and vegetated surfaces, while higher values of r_{ah} (over 100 s/m) are more common during night time (Liu et al., 2006; Liu et al., 2007). Therefore, we proposed the incorporation of a r_{ah} calibration step into the SSEBop model algorithm. This calibration step takes into account the dT_{obs} proposed by Ji et al. (2019) for the dry season, which is when the temperature difference between the hot and cold pixels is higher, due to surface humidity conditions.

4.1.2. SSEBop uncertainty related to input dataset

Calibration of parameter r_{ah} yielded similar results using both meteorological and climatological inputs for the derivation of R_n. Thus, using climatological data to compute dT does not affect ET_a estimates and requires less computational storage, which agrees with Senay et al. (2013). On the other hand, using climatological data to calculate ET_0 and T_c restricts ET_a daily variability and leads to lower estimates during the wet season and, consequently, to a negative bias in annual ET_a. Thus, we found it is best to use daily meteorological data to calculate ET_0 and T_c anomalies. In the absence of daily or hourly meteorological datasets, climatological datasets can be used, after correction of the bias at the annual scale.

4.1.3. SSEBop uncertainty related to c factor zone division

Observations of c factor time series indicate a high correlation with R_n, and a large region split based on latitude provides more accurate c factor seasonality for each split zone. Scene sub-division should, therefore, provide more accurate local ET_a estimations. However, subdivision in too many areas may result in lower c factor standard deviation values, as the viable pixel samples get smaller. Senay et al. (2020) subdivided MODIS images into 5x5 tiles. In our study, even though we used the minimum sample size of 50 pixels (according to Senay et al., 2017), the division of the studied area into 6 zones roughly the same size as the tiles used by Senay et al. (2020) resulted in higher parameter c values. This led to higher ET_a during the dry season, when pixels with NDVI > 0.7 are scarcer and T_{corr} standard deviation is lower (Eqs. (4) and (5)). Therefore, using a minimum of 100 pixels is a more statistically sound threshold to avoid this overestimation (NIST/SEMATECH, 2013; Wan et al., 2014). Scene subdivision should then be adjusted to satisfy this criterion. As a result, larger zones could be necessary in arid and semi-arid climates, where high NDVI pixels are scarcer. Alternatively, c

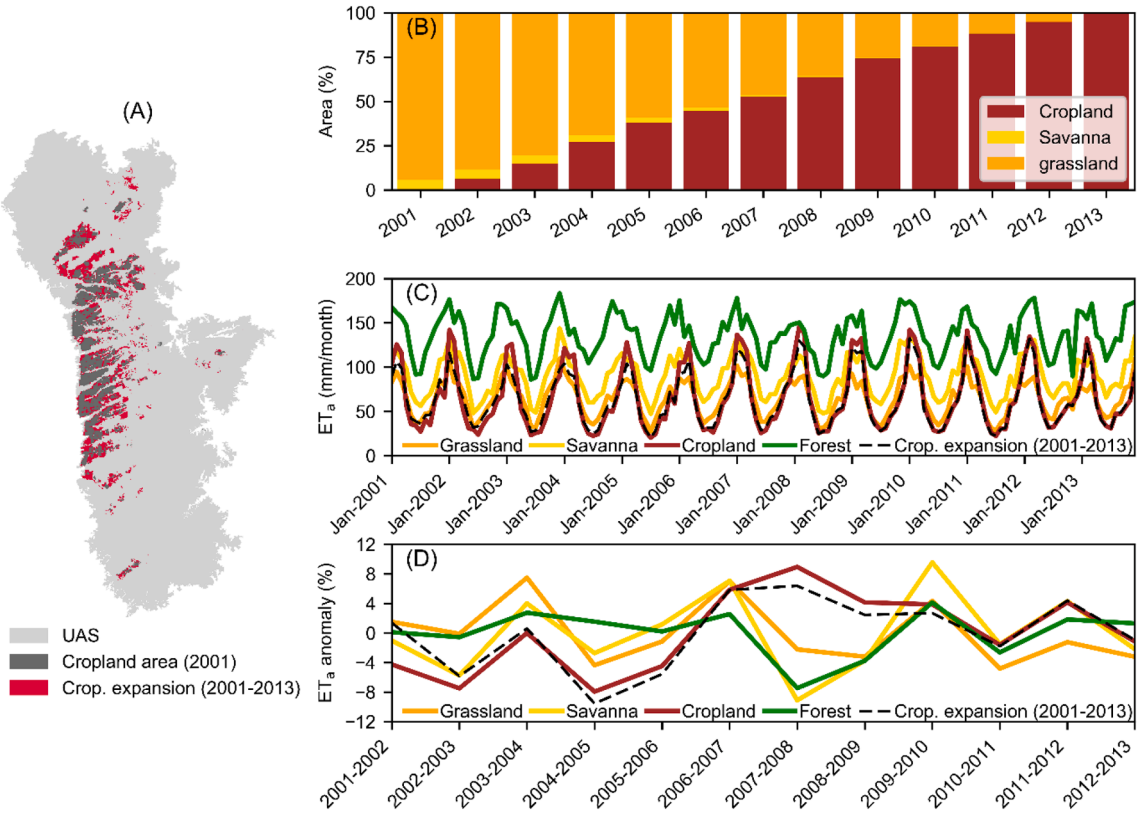

Fig. 9. Cropland expansion in the UAS between 2001 and 2013 (A). Land cover composition evolution within the cropland expansion area (B). SSEBop monthly ET_a for each land cover (spatial averages) in the UAS and in the cropland expansion (2001–2013) area (C). Annual ET_a anomalies per land cover (in relation to each land cover average ET_a, between 2001 and 2013) in the UAS and in the cropland expansion area (D).

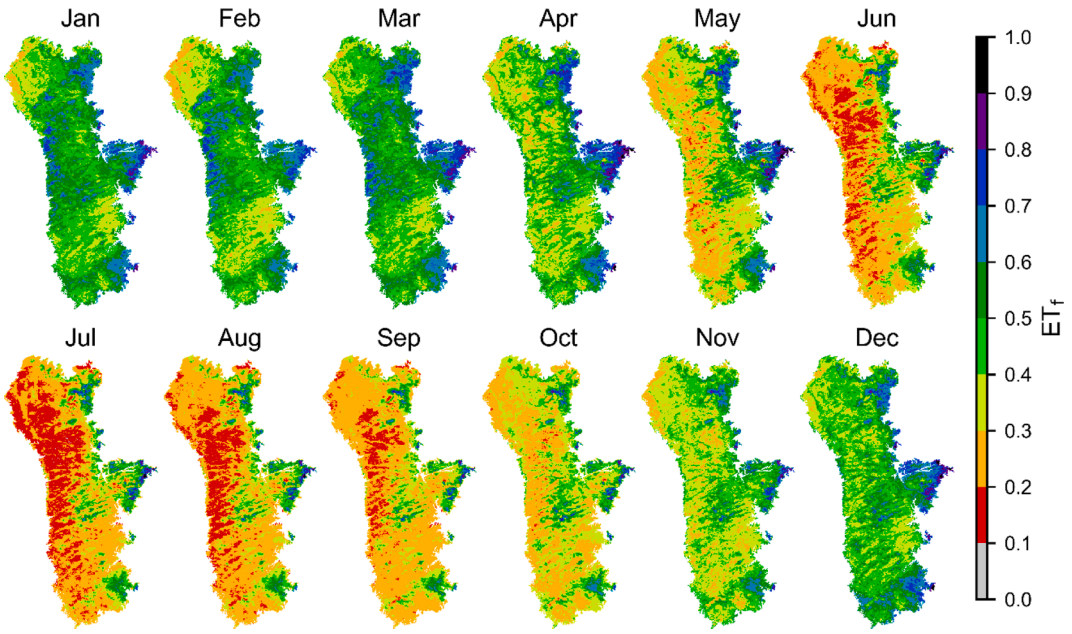

Fig. 10. UAS average monthly SSEBop ET_f (2000–2013).

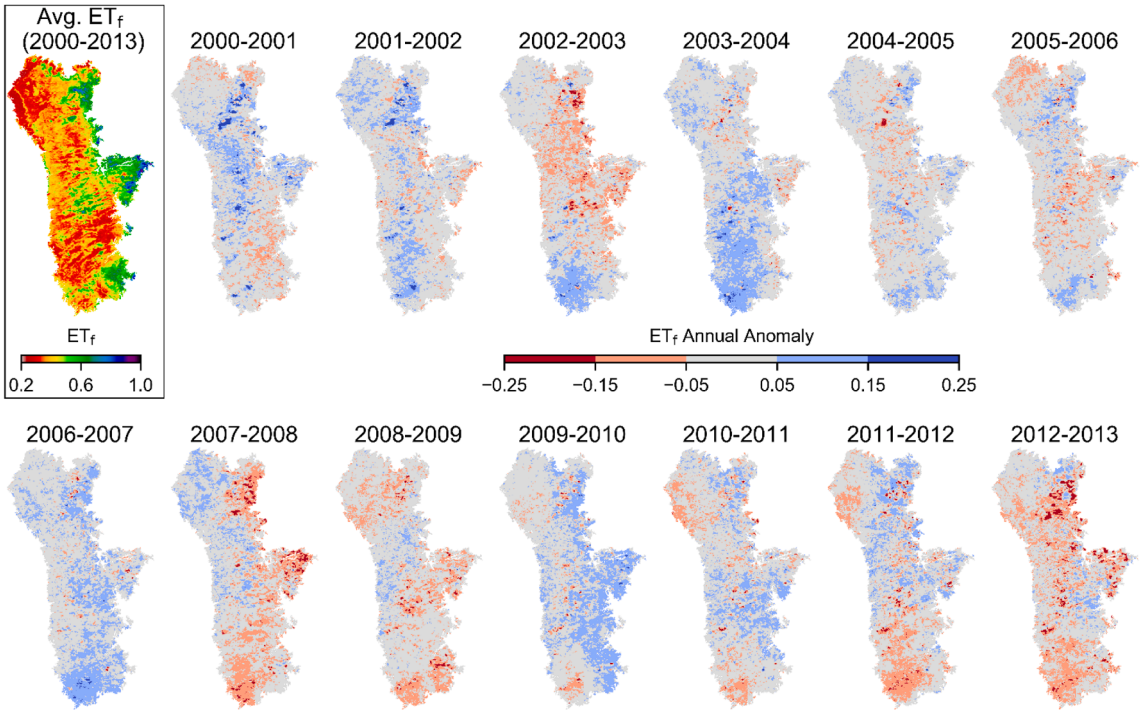

Fig. 11. Average annual SSEBop ET_a and annual anomalies over the UAS.

factor zones division could consider topographic and climatic conditions.

4.1.4. *SSEBop uncertainty related to scaling factor k*

SSEBop ET_a magnitude is greatly influenced by the value of the k factor (Chen et al., 2016). In recent studies, different values of k factor have been used, ranging from 1.00 to 1.25 (Senay et al., 2013; Singh et al., 2013; Senay et al., 2016; Alemayehu et al., 2017; Senay et al., 2017; Chun et al., 2018; Dias Lopes et al., 2019; Paula et al., 2019; Senay et al., 2020); and Senay (2018) recommended a value of k factor value between 1.20 and 1.30, emulating an aerodynamically rougher surface than the grass reference, such as an alfalfa surface. However, the observed k factor of alfalfa lies within a broader range, between 1.15 and 1.70 (Hunsaker et al., 2002; Sharma & Irmak, 2017; Hu et al., 2020), which is expected for climatic conditions that deviate from the standard sub–humid climate (Allen et al., 1998). Although the value of $k = 1.20$ used in this study provided low MD values for SSEBop p5, other values of k factor within the alfalfa range would provide low MD values for other versions too, such as $k = 1.10$ for p6, $k = 1.37$ for p7, and $k = 1.26$ for p8 (obtained via calibration). The k factor should, therefore, be obtained via calibration before SSEBop ET_a usage in water balance applications. For land cover and drought monitoring, however, no calibration is

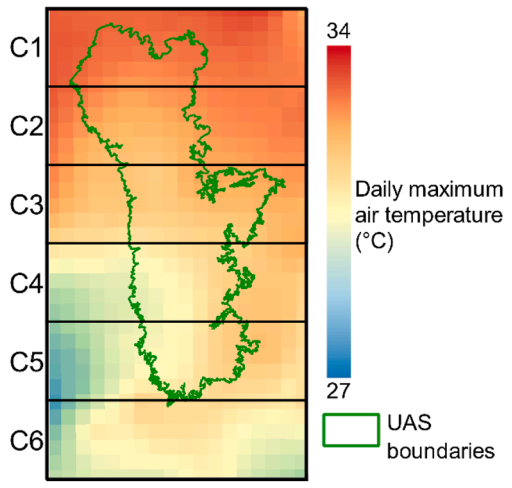

Fig. 12. Spatial division of c factor computation areas and normal (1980–2013) daily maximum air temperature.

needed, as changes in ET_a are more important the its absolute value (Senay et al., 2013).

4.2. Validation of the SSEBop model

At monthly time intervals, SSEBop ET_a estimates presented similar seasonal amplitude to SMAP estimates, version p5 yielding the highest correlation and lowest MAD values. On the other hand, annual SSEBop p5 yielded low correlation to SMAP and WB closure estimates, despite also showing low MD and MAD. Nonetheless, at annual intervals, correlation values are not as important as MD and MAD values, given the low variance of annual ET_a. Converting to daily ET_a, SSEBop p5 yielded MAD values of 0.61 mm/day compared to SMAP monthly estimates and of 0.23 mm/day compared to SMAP and WB closure annual estimates, which are within the average error range of other studies that compare remote sensing models to water balance and local measurements of ET_a (Ruhoff et al., 2012; Senay et al., 2013; Alemayehu et al., 2017; Dias Lopes et al., 2019; Senay et al., 2020).

The main drawback of SSEBop evaluation with basin-scale water balance is the uncertainty of the hydrological model in relation to ET_a estimation. Zhang et al. (2016) showed that WB models present ET_a errors correlated to streamflow errors, with opposite bias. This way, SMAP ET_a uncertainty can be associated to the SMAP average discharge errors of about 10%. On the other hand, other methods of ET_a measurement have similar complications, such as eddy covariance, which presents error in energy balance closure of up to 30% (Twine et al., 2000; Barr et al., 2012; Laipelt et al., 2020). Hence, utilization of hydrological models for remote sensing ET_a validation is considered reasonable and may be used as a surrogate in regions with no ET_a monitoring (Alemayehu et al., 2017), or as a complement in regions where monitoring does not represent the land cover complexity (Ruhoff et al., 2012).

4.3. Land cover and drought monitoring in the UAS

Although no trend in P was identified between 2002 and 2012 in the UAS, both Q and TWSA decreased significantly. This was accompanied by an increase in both ET_0 and ET_a (SMAP and SSEBop). These results agree with what has been found by other studies in the UAS (de Jong et al., 2018; Gonçalves et al., 2019; Pousa et al., 2019). Annual ET_a over cropland land cover correlates positively to ET_0, while natural land covers present an opposite trend. Cropland ET_a also yielded a positive trend between 2002 and 2012, while natural land covers yielded either a negative or no trend. These facts indicate that the presence of croplands, associated with the increase in ET_0, may have been responsible for the decreasing trend of Q and TWSA, between 2002 and 2012.

Drought monitoring in the UAS is proposed in this study via SSEBop ET_f mapping. The ET_f is used instead of the ET_a in the UAS because of the opposite correlation between ET_0 and other hydrological variables, such as P and TWSA, which result in attenuated anomalies of SSEBop ET_a. The ET_f formulation is analogous to that of relative air humidity measured by a psychrometer (Senay, 2018). Thus, while the psychrometer measures air humidity, SSEBop ET_f provides information about land surface humidity. This indicates that the ET_f is a more suitable variable to monitor drought than the ET_a.

5. Conclusions

This study focused on the assessment of the SSEBop model estimates of ET_a and its utilization in understanding the water balance dynamics in the UAS. Given the absence of local measurements of ET_a, SSEBop results were compared to basin-scale estimates from the SMAP monthly model and from annual WB closure, using GRACE measurements of TWSA. This method is a viable alternative for validation in data-scarce areas, as mass conservation is met with low uncertainty (around 10%).

SSEBop ET_a and ET_f estimates were used to monitor land cover change and drought in the UAS, between 2002 and 2012. The expansion of croplands, associated with the increase in ET_0, was identified as the main driver of the decrease in both groundwater and surface water resources of the region, during the studied period.

This paper also provided a comprehensive analysis of the SSEBop model options of parameterization. Based on the comparative evaluation of the eight SSEBop set of parametrizations, the following list of

Table 7
SMAP calibration and validation results.

Calibration Parameters	Discharge Stations							
	FPL		BOQ		FPN		JUV	
k_b ($month^{-1}$)	9.4		6.0		10.9		6.4	
Pe (-)	3.9800		2.8413		3.5246		2.4732	
Str (mm)	6936.9		6474.2		4491.2		8140.3	
Crec	2.9%		9.7%		8.7%		12.0%	
w (-)	0.64		0.23		0.82		0.39	
Initial Conditions	**Calibration**	**Validation**	**Calibration**	**Validation**	**Calibration**	**Validation**	**Calibration**	**Validation**
$T_{u\ ini}$	42.5%	42.5%	38.3%	37.0%	39.5%	40.6%	37.0%	31.0%
$E_{b\ ini}$ (m^3/s)	81.8	66.7	189.0	172.9	144.8	127.0	92.0	77.0
Goal Functions	**Calibration**	**Validation**	**Calibration**	**Validation**	**Calibration**	**Validation**	**Calibration**	**Validation**
NSE	0.74	0.80	0.72	0.88	0.73	0.81	0.68	0.76
R^2	0.78	0.87	0.75	0.89	0.76	0.81	0.71	0.78
Bias	0.9%	1.2%	0.1%	1.3%	−1.5%	−0.9%	2.1%	−2.7%
MAE (mm/month)	10.3 (10.5%)	6.8 (7.8%)	29.1 (11.4%)	18.2 (7.4%)	19.7 (10.6%)	16.2 (9.2%)	13.9 (12.1%)	11.5 (10.7%)
RMSE (mm/month)	13.1 (13.4%)	9.3 (10.6%)	37.4 (14.6%)	25.3 (10.2%)	25.9 (13.9%)	23.2 (13.1%)	19.8 (17.2%)	16.1 (15.1%)

considerations are recommended when implementing the model:

- Comparison of SSEBop dT to observed values of temperature difference demonstrated the necessity of including an internal calibration step of parameter r_{ah} into the coefficient's calculation;
- The use of climatological data does not affect dT results, but it yields lower ET_a estimates in the wet season, causing a biased error. Thus, the use of meteorological data for quantitative studies is recommended. But climatological data still can be used for drought and land cover monitoring, since absolute ET_a values are not necessary for these uses;
- Parameter c spatial zone division is important to ET_a calculation and it should be considered when implementing the SSEBop model over large areas. However, the quantity of split zones is dependent on T_s and NDVI datasets spatial resolution, as well as of the study area's complexity in hydroclimate; and
- The SSEBop scaling factor k plays a major role in ET_a magnitude. Even though the use of a preliminary k factor value is commonly used, calibration of this parameter is necessary before the utilization of SSEBop ET_a estimates in water balance studies.

Given the negative correlation between ET_0 and ET_f in the UAS, SSEBop ET_a yielded attenuated anomalies during dry years. Our results indicate that the SSEBop ET_f is deemed a more suitable tool for drought mapping and monitoring than the SSEBop ET_a.

Funding

The authors would like to acknowledge the Geological Survey of Brazil (CPRM), Brazilian National Water Agency (ANA), Federal University of Minas Gerais (UFMG), Federal University of Rio Grande do Sul (UFRGS), and U.S. Geological Survey (USGS) for the support. The authors would like to gratefully acknowledge the financial support provided by the Brazilian Agency for the Improvement of Higher Education (CAPES) in partnership with the Brazilian National Water Agency (ANA) in the context of the research project "Estimating land surface evapotranspiration using remote sensing models for water management in Brazil", grant number 88881.178687/2018-01. This study was also partially funded by the CAPES under grant number 1577288.

CRediT authorship contribution statement

Bruno César Comini de Andrade: Conceptualization, Methodology, Software, Formal analysis, Writing - original draft, Writing - review & editing, Visualization. **Eber José de Andrade Pinto:** Conceptualization, Methodology, Writing - review & editing, Supervision, Project administration, Funding acquisition. **Anderson Ruhoff:** Conceptualization, Methodology, Writing - review & editing, Supervision, Project administration, Funding acquisition. **Gabriel B. Senay:** Methodology, Writing - review & editing, Supervision.

Declaration of Competing Interest

The authors declare that they have no known competing financial interests or personal relationships that could have appeared to influence the work reported in this paper.

Acknowledgments

Any use of trade, firm, or product names is for descriptive purposes only and does not imply endorsement by the U.S. Government.

Appendix A. SSEBop ET parametrization versions

A.1. Aerodynamic resistance calibration

Despite the recommended value of aerodynamic resistance (r_{ah}) by Senay et al. (2013), it is believed that the implementation of the SSEBop model to other locations other than the United States calls for calibration of the parameter, as errors of 1% in r_{ah} leads to errors of 3% in actual evapotranspiration (ET_a) (Chen et al., 2016).

To calibrate r_{ah}, we used a method for the calculation of the observed temperature difference (dT_{obs}), defined by Ji et al. (2019), based on the choice of hot and cold pixels. Hot pixels are defined as Normalized Difference Vegetation Index (NDVI) < 0.25 and cold pixels as NDVI > 0.70. dT_{obs} values are computed as the average difference between hot and cold pixels, in each scene. In order to compare surface temperature from different locations, T_s needs to be corrected for elevation, as presented by Eq. (10)

$$T_{s,corrected} = LR \times z + T_s \tag{10}$$

where $T_{s,\ corrected}$ is the elevation-corrected surface temperature; LR is the lapse rate at which temperature decreases with an increase in elevation; z is the surface elevation; and T_s is the MODIS surface temperature. As Ji et al. (2019), we used a constant LR of 0.0065 K/m.

Observed dT sampling was done for the entire UAS region. To avoid outliers in the $T_{s,\ corrected}$, a minimum of 100 pixels was established as necessary for both hot and cold temperature computations. dT_{obs} was calculated by Eq. (11):

$$dT_{obs} = T_{h,obs} - T_{c,obs} \tag{11}$$

where dT_{obs} is observed dT for each day; $T_{h,\ obs}$ and $T_{c,\ obs}$ are average temperature of hot and cold pixels, respectively.

Calibration of r_{ah} was performed to reduce quadratic errors between dT_{obs} and dT. For the calibration, only the driest months were considered (May to September), as they more reliably represent the temperature difference between a dry surface and a wet one.

A.2. Input dataset selection

In order to assess the difference between running SSEBop with daily meteorological data against using average climatological data, the model was applied considering both for dT, T_c, and ET_0. Meteorological data were used as provided by Xavier et al. (2015). From this dataset, climatological data (T_{max}, T_{min} and ET_0) were derived as the average for each 6-day period of the year. The datasets are available from 1980 to 2017. However, due to the non-stationarity identified in the T_{max} and ET_0 time series, only the period between 2000 and 2013 was used.

A.3. Parameter c factor zone division

Although SSEBop eliminates the subjective selection of cold and hot boundaries, the model parameters required improvements as more research was employed. Senay et al. (2017) and Alemayehu et al. (2017) identified the need of a seasonally variable coefficient c, and Senay et al. (2020) proposed the division of MODIS tiles into 5 by 5 sub-tiles, to account for spatial variability.

In this paper, two methods of c calculation are proposed: one derived for the whole UAS region; and another in which the UAS was split into zones, based on latitude. Due to the climatological conditions and large latitudinal range of the study area, the second method involved the sub-division of the region into 6 zones distributed along the north–south axis, each with an area of approximately 66,000 km^2, as shown in Fig. 12. The daily maximum air temperature is presented as well, as the climatological normal between 1980 and 2013 (extracted from the data provided by Xavier et al., 2015). A clear slope can be observed, with higher temperatures in the north (C1) and lower temperatures in the south (C6).

Appendix B. Water balance-based ET calculation procedures

B.1. SMAP ET calculation procedure

The Soil Moisture Accounting Procedure (SMAP) is a lumped conceptual rainfall-runoff model, developed by Lopes et al. (1982). It was initially designed for daily forecasts, but hourly and monthly versions have also been presented, with modifications in the model's structure (Alexandre et al., 2013; Fernández Bou et al., 2015). SMAP has been widely used within various Brazilian basins, with minor adaptations in its structure and transfer functions (Nunes et al., 2014; Campos et al., 2018; Silva et al., 2019). Model validation has proven its efficiency is comparable to other more widely known models, such as the ABCD (Block et al., 2009).

In this study, a monthly version of SMAP was used. This version is composed of two reservoirs that represent the saturated (R_{sub}) and unsaturated (R_{solo}) zones. Spatial averages of precipitation and potential evapotranspiration were used as input and observed streamflow was used for calibration.

For each time-step, the two reservoir volumes and transference functions are described by Eqs. (12)–(21):

Mathematical Reservoirs:

$$R_{solo}(1) = Tu(1) \cdot Str \tag{12}$$

$$R_{sub}(1) = \frac{BF(1) \cdot Uu}{(1 - 0.5^{\frac{1}{k_b}}) \cdot DA} \tag{13}$$

$$R_{solo}(t) = R_{solo}(t-1) + P(t) - E_s(t) - ET_a(t) - Rec(t) \tag{14}$$

$$R_{sub}(t) = R_{sub}(t-1) + Rec(t) - E_b(t) \tag{15}$$

Transference Functions:

$$Tu(t) = \frac{R_{solo}(t)}{Str} \tag{16}$$

$$E_s(t) = P'(t) \cdot Tu(t)^{Pes} \tag{17}$$

$$ET_a(t) = Tu(t) \cdot ET_p(t) \tag{18}$$

$$Rec(t) = Crec \cdot R_{solo}(t) \cdot Tu(t)^4 \tag{19}$$

$$E_b(t) = R_{sub}(t) \cdot (1 - 0.5^{\frac{1}{k_b}}) \tag{20}$$

$$Q(t) = \frac{[E_s(t) + E_b(t)] \cdot DA}{Uu} \tag{21}$$

where $R_{solo}(1)$ is the initial soil reservoir volume (mm); $R_{sub}(1)$ is the initial groundwater reservoir volume (mm); $R_{solo}(t)$ is the soil reservoir volume at the start of time-step t (mm); $R_{sub}(t)$ is the groundwater reservoir volume at the start of time-step t (mm); P(t) is precipitation during time-step t (mm); $ET_p(t)$ is potential evapotranspiration during time-step t (mm); $E_s(t)$ is runoff during time-step t (mm); $ET_a(t)$ is actual evapotranspiration during time-step t (mm); Rec(t) is groundwater recharge during time-step t (mm); $E_b(t)$ is baseflow during time-step t (mm); Q(t) is total streamflow ($m^3 s^{-1}$); Tu(t) is soil moisture ratio (dimensionless); BF(1) is initial baseflow ($m^3 s^{-1}$); DA is the river basin drainage area (km^2); Uu is unit conversion coefficient (Uu = 2629.8 month). The model calibration parameters are: soil saturation capacity, Str (mm); runoff parameter, Pes (dimensionless); recession coefficient, k_b (dimensionless); and groundwater recharge coefficient, Crec (dimensionless).

Two optimization procedures were applied to the model calibration. In order to consider eventual accumulations of water on superficial water bodies, the computation of E_s (t) (Eq. (17)) was done considering the averaged value of precipitation, described by Eq. (22)

$$P'^{(t)} = P(t) \times w + P(t-1) \times (1 - w) \tag{22}$$

where w is month precipitation weight (dimensionless), between 0 and 1, which states that past month precipitation may influence streamflow. The value of w is obtained by calibration.

Additionally, the well-known Heun's numerical method was applied to reduce errors introduced by the large monthly time-steps. This way, to estimate the R_{solo} and R_{sub} reservoirs depths, Eqs. (14) and (15) are substituted by Eqs. (23) and (24):

$$R_{solo}(t) = R_{solo}(t-1) + \frac{\Delta R_{solo}(t)^* + \Delta R_{solo}(t+1)^*}{2} \tag{23}$$

$$R_{sub}(t) = R_{sub}(t-1) + \frac{\Delta R_{sub}(t)^{*} + \Delta R_{sub}(t+1)^{*}}{2} \quad (24)$$

where $\Delta R_{solo}(t)^*$ and $\Delta R_{solo}(t+1)^*$ are temporary values of $P - E_s - ET_a - Rec$ for time-steps t and $t+1$, respectively; $\Delta R_{sub}(t)^*$ and $\Delta R_{sub}(t+1)^*$ are temporary values of $Rec - E_b$ for time-steps t and $t+1$, respectively.

Model calibration was applied by employing a global efficiency coefficient (GEC), given by Eq. (25):

$$GEC = (1 - R^2) + 2 \cdot |\%Bias| + 3 \cdot \%RMSE + 4 \cdot \%MAE + 5 \cdot |NSE - 1| \quad (25)$$

where R^2 is the determination coefficient (dimensionless); |%Bias| is the absolute value of the mean error between simulated and observed streamflow, relative to average observed flow (dimensionless); %RMSE is root mean square error, relative to average observed flow (dimensionless); MAE is mean absolute error, relative to average observed flow (dimensionless); and NSE is the Nash-Sutcliffe coefficient (Nash & Sutcliffe, 1970).

Primarily, an automatic calibration algorithm was employed to adjust the Str, Pes, k_b and Crec. Tu(1) and BF(1) values were then determined to minimize errors in the earlier simulation months. Finally, month weights were calibrated to optimize GEC value. These iterations were repeated until convergence was reached for GEC.

Uncertainty of SMAP ET_a estimates was derived based on the correlation between modeled streamflow and modeled ET_a biases found by Zhang et al. (2016). ET_a uncertainty was calculated monthly as the 95% confidence interval of monthly flow biases, multiplied by the ET_a over streamflow ratio.

Table 7 displays SMAP input parameters and initial conditions resulting from calibration, as well as the performance indicators (Goal Functions) of the calibration and validation periods. In the validation series, NSE varied between 0.68 and 0.88, R^2 between 0.71 and 0.89. Absolute bias stayed below 3.0%, while maximum MAE and RMSE were found for JUV, at 12.1% and 17.2%, respectively.

B.2. Water balance closure calculation procedure

ET_a was also derived from the annual water balance for each river basin, using Eq. (26).

$$ET_a(t) = P(t) - Q(t) - \Delta S(t) \quad (26)$$

where ET_a is annual evapotranspiration rate; P is annual precipitation; Q is annual flow; and ΔS is of terrestrial water storage annual variation, derived from Eq. (27)

$$\Delta S(t) = TWSA(t+1) - TWSA(t) \quad (27)$$

where TWSA is GRACE annual terrestrial water storage anomaly. GRACE TWSA was generated as a mean of the three available products: Center for Space Research (CSR), Jet Propulsion Laboratory (JPL), and GeoForschungsZentrum (GFZ), which, according to Sakumura et al. (2014), produces less noise and improves accuracy, in comparison to using a single product.

References

Alemayehu, T., van Griensven, A., Senay, G.B., Bauwens, W., 2017. Evapotranspiration Mapping in a Heterogeneous Landscape Using Remote Sensing and Global Weather Datasets: Application to the Mara Basin, East Africa. *Remote Sensing* 9 (4), 390. https://doi.org/10.3390/rs9040390.

Alexandre, A.M.B., et al., 2013. Incorporação do Impacto da Rede de Reservatórios Superficiais Artificiais de Caráter Intranual na Modelagem Hidrológica Chuva-Vazão. Revista Brasileira de Recursos Hídricos 12 (2), 67–82.

Allen, R.G., Pereira, L.S., Raes, D., Smith, M., 1998. Crop EvapoTranspiration: Guidelines for Computing Crop Water Requirements. In: United Nations FAO, Irrigation and Drainage Paper 56. FAO, Rome, Italy.

Alley, W.M., 1984. On the Treatment of Evapotranspiration, Soil Moisture Accounting, and Aquifer Recharge in Monthly Water Balance Models. Water Resour. Res. 20 (8), 1137–1149. https://doi.org/10.1029/wr020i008p01137.

Althoff, D., Rodrigues, L.N., da Silva, D.D., 2019. Evaluating Evaporation Methods for Estimating Small Reservoir Water Surface Evaporation in the Brazilian Savannah. Water 11 (9), 1942. https://doi.org/10.3390/w11091942.

Alvares, C.A., Stape, J.L., Sentelhas, P.C., de Moraes Gonçalves, J.L., Sparovek, G., 2013. Köppen's climate classification map for Brazil. Meteorol. Z. 22 (6), 711–728. https://doi.org/10.1127/0941-2948/2013/0507.

ANA – Agência Nacional de Águas, 2017. Atlas Irrigação: Uso da Água na Agricultura Irrigada. ANA, Brasília.

ANA, 2018. Conjuntura dos Recursos Hídricos no Brasil 2018: Informe Anual. ANA, Brasília.

ANA, 2019. Levantamento da Agricultura Irrigada por Pivôs Centrais no Brasil. ANA, Brasília.

Barr, A.G., van der Kamp, G., Black, T.A., McCaughey, J.H., Nesic, Z., 2012. Energy balance closure at the BERMS flux towers in relation to the water balance of the White Gull Creek watershed 1999–2009. Agric. For. Meteorol. 153, 3–13. https://doi.org/10.1016/j.agrformet.2011.05.017.

Bazame, H., Althoff, D., Filgueiras, R., Alves, E., 2018. Rainfall spatio-temporal distribution of Western Bahia. Water Resour. Irrigat. Manage. 7 (2–3).

Block, P.J., et al., 2009. Streamflow Forecasting Framework Using Multiple Climate and Hydrological Models. J. Am. Water Resour. Assoc. 25 (4), 828–843.

Campos, D.O., Dos Santos, J.W.B., DE Assis, P.B., 2018. Application of the SMAP hydrological model in the determination of water production in a coastal watershed. Revista Brasileira de Geografia Física 11 (1), 124–138.

Chen, J.L., Wilson, C.R., Tapley, B.D., Yang, Z.L., Niu, G.Y., 2009. 2005 drought event in the Amazon River basin as measured by GRACE and estimated by climate models. J. Geophys. Res. 114 (B5) https://doi.org/10.1029/2008jb006056.

Chen, M., Senay, G.B., Singh, R.K., Verdin, J.P., 2016. Uncertainty analysis of the Operational Simplified Surface Energy Balance (SSEBop) model at multiple flux tower sites. J. Hydrol. 536, 384–399. https://doi.org/10.1016/j.jhydrol.2016.02.026.

Chun, J.A., Baik, J., Kim, D., Choi, M., 2018. A comparative assessment of SWAT-model-based evapotranspiration against regional-scale estimates. Ecological Engineering 122, 1–9. https://doi.org/10.1016/j.ecoleng.2018.07.015.

Danielson, J.J., Gesch, D.B., 2011, Global multi-resolution terrain elevation data 2010 (GMTED2010), U.S. Geological Survey Open-File Report 2011–1073, pp. 26.

De Jong, P., Tanajura, C.A.S., Sánchez, A.S., Dargaville, R., Kiperstok, A., Torres, E.A., 2018. Hydroelectric production from Brazil's São Francisco River could cease due to climate change and inter-annual variability. Sci. Total Environ. 634, 1540–1553. https://doi.org/10.1016/j.scitotenv.2018.03.256.

De Sales, F., Rother, D.E., 2020. A New Coupled Modeling Approach to Simulate Terrestrial Water Storage in Southern California. Water 12 (3), 808. https://doi.org/10.3390/w12030808.

Dias Lopes, J., Neiva Rodrigues, L., Acioli Imbuzeiro, H.M., Falco Pruski, F., 2019. Performance of SSEBop model for estimating wheat actual evapotranspiration in the Brazilian Savannah region. Int. J. Remote Sens. 1–18 https://doi.org/10.1080/01431161.2019.1597304.

Didan, K., 2015. MOD13A2 MODIS/Terra Vegetation Indices 16-Day L3 Global 1km SIN Grid V006. NASA EOSDIS Land Processes DAAC. Available at: <https://doi.org/10.5067/modis/mod13a2.006> (access: 15 Feb. 2019).

Fernández Bou, A.S., Ventura De Sá, R., Cataldi, M., 2015. Flood forecasting in the upper Uruguay River basin. Nat. Hazards 79, 1239–1256.

Fisher, J.B., Melton, F., Middleton, E., Hain, C., Anderson, M., Allen, R., McCabe, M.F., Hook, S., Baldocchi, D., Townsend, P.A., Kilic, A., Tu, K., Miralles, D.D., Perret, J., Lagouarde, J., Waliser, D., Purdy, A.J., French, A., Schimel, D., Famiglietti, J.S., Stephens, G., Wood, E.F., 2017. The future of evapotranspiration: Global

requirements for ecosystem functioning, carbon and climate feedbacks, agricultural management, and water resources. Water Resour. Res. 53, 2618–2626. https://doi.org/10.1002/2016WR020175.
Friedl, M., Sulla-Menashe, D., 2019. MCD12Q1 MODIS/Terra+Aqua Land Cover Type Yearly L3 Global 500m SIN Grid V006 . NASA EOSDIS Land Processes DAAC. Accessed 2020-07-18 from https://doi.org/10.5067/MODIS/MCD12Q1.006.
Fu, Y., Argus, D.F., Freymueller, J.T., Heflin, M.B., 2013. Horizontal motion in elastic response to seasonal loading of rain water in the Amazon Basin and monsoon water in Southeast Asia observed by GPS and inferred from GRACE. Geophys. Res. Lett. 40 (23), 6048–6053. https://doi.org/10.1002/2013gl058093.
Gaspar, M.T.P., Campos, J.E.G., 2007. O Sistema Aquífero Urucuia. Revista Brasileira de Geociências 37 (4), 216–226.
Gonçalves, R.D., Engelbrecht, B.Z., Chang, H.K., 2018. Evolução da contribuição do Sistema Aquífero Urucuia para o Rio São Francisco Brasil. Águas Subterrâneas 32 (1), 1–10.
Gonçalves, R.D., Stollberg, R., Weiss, H., Chang, H.K., 2019. Using GRACE to quantify the depletion of terrestrial water storage in Northeastern Brazil: The Urucuia Aquifer System. Sci. Total Environ. 135845 https://doi.org/10.1016/j.scitotenv.2019.135845.
Guimarães, D., et al., 2017. Diagnóstico da Agricultura Irrigada no Extremo Oeste Baiano. In: Congresso Brasileiro de Agrometeorologia, 20, 2017. Petrolina/Juazeiro, pp. 2710–2720.
Guo, D., Westra, S., Maier, H.R., 2017. Impact of evapotranspiration process representation on runoff projections from conceptual rainfall-runoff models. Water Resour. Res. 53 (1), 435–454. https://doi.org/10.1002/2016wr019627.
Hu, Y., Kang, S., Ding, R., Du, T., Tong, L., Li, S., 2020. The Dynamic Yield Response Factor of Alfalfa Improves the Accuracy of Dual Crop Coefficient Approach under Water and Salt Stress. Water 12 (5), 1224. https://doi.org/10.3390/w12051224.
Hunsaker, D.J., Pinter Jr., P.J., Cai, H., 2002. Alfalfa Basal Crop Coefficients for FAO-56 Procedures in the Desert Regions of the Southwestern U.S. Transactions of the ASAE 45 (6). https://doi.org/10.13031/2013.11431.
INMET – Instituto Nacional de Meteorologia, 2019. Normais Climatológicas do Brasil. Available: http://www.inmet.gov.br/portal/index.php?r=clima/normaisClimatologicas (access on: 01 Aug. 2019).
Ji, L., Senay, G.B., Velpuri, N.M., Kagone, S., 2019. Evaluating the Temperature Difference Parameter in the SSEBop Model with Satellite-Observed Land Surface Temperature Data. Remote Sens. 11 (16), 1947. https://doi.org/10.3390/rs11161947.
Kalma, J.D., McVicar, T.R., McCabe, M.F., 2008. Estimating Land Surface Evaporation: A Review of Methods Using Remotely Sensed Surface Temperature Data. Surv. Geophys. 29 (4–5), 421–469. https://doi.org/10.1007/s10712-008-9037-z.
Laipelt, L., Ruhoff, A.L., Fleischmann, A.S., Kayser, R.H.B., Kich, E.de M., da Rocha, H.R., Neale, C.M.U., 2020. Assessment of an Automated Calibration of the SEBAL Algorithm to Estimate Dry-Season Surface-Energy Partitioning in a Forest-Savanna Transition in Brazil. Remote Sens. 12 (7), 1108. https://doi.org/10.3390/rs12071108.
Li, Z.L., Tang, R., Wan, Z., Bi, Y., Zhou, C., Tang, B., Yan, G., Zhang, X., 2009. A review of current methodologies for regional evapotranspiration estimation from remotely sensed data. *Sensors* (Basel, Switzerland) 9 (5), 3801–3853. https://doi.org/10.3390/s90503801.
Liou, Y.-A., Kar, S., 2014. Evapotranspiration Estimation with Remote Sensing and Various Surface Energy Balance Algorithms—A Review. Energies 7 (5), 2821–2849. https://doi.org/10.3390/en7052821.
Liu, S., Mao, D., Lu, L., 2006. Measurement and estimation of the aerodynamic resistance. Hydrol. Earth Syst. Sci. Discuss. Eur. Geosci. Union 3 (3), 681–705 ffhal00298684.
Liu, S., Lu, L., Mao, D., Jia, L., 2007. Evaluating parameterizations of aerodynamic resistance to heat transfer using field measurements. Hydrol. Earth Syst. Sci. 11 (2), 769–783. https://doi.org/10.5194/hess-11-769-2007.
Lopes, J.E.G., Braga Jr., B.P.F., Conejo, J.G.L., 1982. SMAP - A Simplified Hydrological Model. In: Singh, V.P. (Ed.), Applied Modelling in Catchment Hydrology. Water Resources Publications.
Moreira, A.A., Ruhoff, A.L., Roberti, D.R., de Arruda Souza, V., da Rocha, H.R., de Paiva, R.C.D., 2019. Assessment of terrestrial water balance using remote sensing data in *South America*. J. Hydrol. https://doi.org/10.1016/j.jhydrol.2019.05.021.
Nahmani, S., Bock, O., Bouin, M.-N., Santamaría-Gómez, A., Boy, J.-P., Collilieux, X., Métivier, L., Panet, I., Genthon, P., de Linage, C., Wöppelmann, G., 2012. Hydrological deformation induced by the West African Monsoon: Comparison of GPS, GRACE and loading models. J. Geophys. Res. Solid Earth 117 (B5). https://doi.org/10.1029/2011jb009102.
Nash, J.E., Sutcliffe, J.V., 1970. River Flow Forecasting Through Conceptual Models, Part I – A Discussion of Principles. J. Hydrol. 10, 282–290.
NIST/SEMATECH, 2013. e-Handbook of Statistical Methods, retrieved November 15, 2020 from http://www.itl.nist.gov/div898/handbook/. doi: https://doi.org/10.18434/M32189.
Nunes, F.M.S., et al., 2014. Modelagem hidrológica via SMAP para estimativa de vazões mensais na bacia do rio Piancó. Revista Verde de Agroecologia e Desenvolvimento Sustentável 9 (3), 289–295.
Opoku-Duah, S., Donoghue, D., Burt, T., 2008. Intercomparison of Evapotranspiration Over the Savannah Volta Basin in West Africa Using Remote Sensing Data. Sensors 8 (4), 2736–2761. https://doi.org/10.3390/s8042736.
de Paula, A.C.P., da Silva, C.L., Rodrigues, L.N., Schererwarren, M., 2019. Performance of the SSEBop model in the estimation of the actual evapotranspiration of soybean and bean crops. Pesquisa Agropecuária Brasileira 54, e00739. https://doi.org/10.1590/S1678-3921.pab2019.v54.00739.
Pousa, Costa, Pimenta, Fontes, Brito, Castro, 2019. Climate Change and Intense Irrigation Growth in Western Bahia, Brazil: The Urgent Need for Hydroclimatic Monitoring. Water 11 (5), 933. https://doi.org/10.3390/w11050933.
Ruhoff, A., Paz, A., Collischonn, W., Aragão, L., Rocha, H., Malhi, Y., 2012. A MODIS-Based Energy Balance to Estimate Evapotranspiration for Clear-Sky Days in Brazilian Tropical Savannas. Remote Sens. 4 (3), 703–725. https://doi.org/10.3390/rs4030703.
Sakumura, C., Bettadpur, S., Bruinsma, S., 2014. Ensemble prediction and intercomparison analysis of GRACE time-variable gravity field models. Geophys. Res. Lett. 41 (5), 1389–1397. https://doi.org/10.1002/2013gl058632.
Schmidt, T., et al., 2008. Hydrological Signals Observed by the GRACE Satellites. Surv. *Geophys* 2008 (29), 319–334.
Senay, G.B., Bohms, S., Singh, R.K., Gowda, P.H., Velpuri, N.M., Alemu, H., Verdin, J.P., 2013. Operational Evapotranspiration Mapping Using Remote Sensing and Weather Datasets: A New Parameterization for the SSEB Approach. JAWRA J. Am. Water Resour. Assoc. 49 (3), 577–591. https://doi.org/10.1111/jawr.12057.
Senay, G.B., Friedrichs, M., Singh, R.K., Velpuri, N.M., 2016. Evaluating Landsat 8 evapotranspiration for water use mapping in the Colorado River Basin. Remote Sensing of Environment 185, 171–185. https://doi.org/10.1016/j.rse.2015.12.043.
Senay, G.B., Schauer, M., Friedrichs, M., Velpuri, N.M., Singh, R.K., 2017. Satellite-based water use dynamics using historical Landsat data (1984–2014) in the southwestern United States. Remote Sens. Environ. 202, 98–112. https://doi.org/10.1016/j.rse.2017.05.005.
Senay, G.B., 2018. Satellite Psychrometric Formulation of the Operational Simplified Surface Energy Balance (SSEBop) Model for Quantifying and Mapping Evapotranspiration. Appl. Eng. Agric. 34 (3), 555–566. https://doi.org/10.13031/aea.12614.
Senay, G.B., Kagone, S., Velpuri, N.M., 2020. Operational Global Actual Evapotranspiration: Development, Evaluation, and Dissemination. Sensors 20 (7), 1915. https://doi.org/10.3390/s20071915.
Sharma, V., Irmak, S., 2017. Soil-Water Dynamics, Evapotranspiration, and Crop Coefficients of Cover-Crop Mixtures in Seed Maize Cover-Crop Rotation Fields. II: Grass-Reference and Alfalfa-Reference Single (Normal) and Basal Crop Coefficients. J. Irrig. Drain. Eng. 143 (9), 04017033. https://doi.org/10.1061/(asce)ir.1943-4774.0001215.
Silva, F.P.R., Alves, J.L.D., Cataldi, M., 2019. Climate downscaling over South America for 1971–2000: application in SMAP rainfall-runoff model for Grande River Basin. Clim. Dyn. 52, 681–696.
Singh, R., Senay, G., Velpuri, N., Bohms, S., Scott, R., Verdin, J., 2013. Actual Evapotranspiration (Water Use) Assessment of the Colorado River Basin at the Landsat Resolution Using the Operational Simplified Surface Energy Balance Model. Remote Sensing 6 (1), 233–256. https://doi.org/10.3390/rs6010233.
Sun, T., Ferreira, V., He, X., Andam-Akorful, S., 2016. Water Availability of São Francisco River Basin Based on a Space-Borne Geodetic Sensor. Water 8 (5), 213. https://doi.org/10.3390/w8050213.
Swenson, S.C., 2012. GRACE monthly land water mass grids NETCDF RELEASE 5.0. Ver. 5.0. PO.DAAC, CA, USA. Dataset accessed [2019-11-15] at https://doi.org/10.5067/TELND-NC005.
Tapley, B.D., et al., 2004. The gravity recovery and climate experiment: Mission overview and early results. Geophys. Res. Lett. 31, 4 p.
Tateishi, R., Ahn, C.H., 1996. Mapping evapotranspiration and water balance for global land surfaces. ISPRS J. Photogramm. Remote Sens. 51 (4), 209–215. https://doi.org/10.1016/0924-2716(96)00015-9.
Twine, T.E., Kustas, W.P., Norman, J.M., Cook, D.R., Houser, P.R., Meyers, T.P., et al., 2000. Correcting eddy-covariance flux underestimates over a grassland. Agric. For. Meteorol. 103 (3), 279–300. https://doi.org/10.1016/s0168-1923(00)00123-4.
Wan, X., Wang, W., Liu, J., Tong, T., 2014. Estimating the sample mean and standard deviation from the sample size, median, range and/or interquartile range. BMC Med. Res. Method. 14 (1) https://doi.org/10.1186/1471-2288-14-135.
Wouters, B., Bonin, J.A., Chambers, D.P., Riva, R.E.M., Sasgen, I., Wahr, J., 2014. GRACE, time-varying gravity, Earth system dynamics and climate change. Rep. Prog. Phys. 77 (11), 116801 https://doi.org/10.1088/0034-4885/77/11/116801.
Xavier, L., Becker, M., Cazenave, A., Longuevergne, L., Llovel, W., Filho, O.C.R., 2010. Interannual variability in water storage over 2003–2008 in the Amazon Basin from GRACE space gravimetry, in situ river level and precipitation data. Remote Sens. Environ. 114 (8), 1629–1637. https://doi.org/10.1016/j.rse.2010.02.005.
Xavier, A.C., King, C.W., Scanlon, B.R., 2015. Daily gridded meteorological variables in Brazil (1980–2013). Int. J. Climatol. 36 (6), 2644–2659. https://doi.org/10.1002/joc.4518.
Yue, S., Wang, C., 2004. The Mann-Kendall test modified by effective sample size to detect trend in serially correlated hydrological series. Water Resour. Manage. 18 (3), 201–218. https://doi.org/10.1023/B:WARM.0000043140.61082.60.
Zhang, Y., Zheng, H., Chiew, F.H.S., Arancibia, J.P., Zhou, X., 2016. Evaluating Regional and Global Hydrological Models against Streamflow and Evapotranspiration Measurements. J. Hydrometeorol. 17 (3), 995–1010. https://doi.org/10.1175/jhm-d-15-0107.1.
Z. Wan, S.H., 2015 MOD11A1 MODIS/Terra Land Surface Temperature/Emissivity Daily L3 Global 1km SIN Grid V006. NASA EOSDIS Land Processes DAAC. Available at <https://doi.org/10.5067/modis/mod11a1.006> (access: 15 Feb. 2019).